Impact of the plastic deformation microstructure in metals on the kinetics of recrystallization: A phase-field study

Ahmed Hamed[a,1], Rayaprolu Goutham Sreekar Annadanam[a,2], Grethe Winther[b], and Anter El-Azab[a,2]

[a] School of Materials Engineering, Purdue University, West Lafayette, IN 47907, USA

[b] Department of Civil and Mechanical Engineering, Technical University of Denmark, DK-2800 Kgs. Lyngby, Denmark

Abstract

The sensitivity of recrystallization kinetics in metals to the heterogeneity of microstructure and deformation history is a widely accepted experimental fact. However, most of the available recrystallization models employ either a mean field approach or use grain-averaged parameters, and thus neglecting the mesoscopic heterogeneity induced by prior deformation. In the present study, we investigate the impact of deformation-induced dislocation (subgrain) structure on the kinetics of recrystallization in metals using the phase-field approach. The primary focus here is upon the role of dislocation cell boundaries. The free energy formulation of the phase-field model accounts for the heterogeneity of the microstructure by assigning localized energy to the resulting dislocation microstructure realizations generated from experimental data. These microstructure realizations are created using the universal scaling laws for the spacing and the misorientation angles of both the geometrically necessary and incidental dislocation boundaries. The resulting free energy is used into an Allen-Cahn based model of recrystallization kinetics, which are solved using the finite element method. The solutions thus obtained shed light on the critical role of the spatial heterogeneity of deformation in the non-smooth growth of recrystallization nuclei and on the final grain structure. The results showed that, in agreement with experiment, the morphology of recrystallization front exhibits protrusions and retrusions. By resolving the subgrain structure, the presented algorithm paves the way for developing predictive kinetic models that fully account for the deformed state of recrystallizing metals.

[1] Current address: Energy and Environmental Science and Technology Directorate, Idaho National Laboratory, Idaho Falls, ID, USA

[2] Corresponding authors: arayapro@purdue.edu, aelazab@purdue.edu

1. Introduction

Thermomechanical treatment has been widely used to control the microstructure, texture, and properties of metals and alloys in industrial processes. Customarily, this starts by work hardening the material via mechanical deformation, followed by thermal annealing at high temperature [1–5]. During plastic deformation, a small fraction of the mechanical energy is stored in the form of crystalline defects, mainly dislocations, while the rest is released in the form of heat [6]. On the other hand, annealing leads to microstructural changes driven by stored energy minimization. Stored energy release occurs mainly by three mechanisms: recovery, recrystallization, and grain coarsening [1,5]. Microscopically, these mechanisms comprise rearrangement and annihilation of crystal defects and can take place simultaneously or at different timescales. Recovery includes all processes that do not require high angle grain boundaries movement [6–9]. Grain coarsening, on the other hand, is the growth of the mean grain size driven by the reduction in grain boundary area. Recrystallization is the intermediate mechanism and can be defined as the formation and migration of high angle grain boundaries (with misorientation angle > 10-15^0) driven by the stored energy of deformation [10–16]. Recrystallization consists of two stages, nucleation and growth, and ends by eliminating almost all the dislocations induced by the plastic deformation.

Several models exist to capture the recrystallization phenomena, including mainly analytical and mesoscale approaches. Analytical methods employing mean-field approach, such as Johnson-Mehl-Avrami-Kolmogorov (JMAK) and its extensions or the cellular stability model [5,17,18], give mainly a qualitative description of recrystallization behavior that can provide some insights about recrystallization kinetics. Meanwhile, pursuing mesoscopic approaches for quantitative prediction of microstructural evolution during recrystallization of a given deformed state sounds achievable. In this regard, several techniques are sought to handle the spatial complexity of the problem [18–33]. Each of these topological models has its own capabilities and limitations. Monte

Carlo (Potts model) approach [5,18–20] and phase-field modeling [25–36] are among the leading models. Cellular automata models [5,19,24] are closely related to the Potts model with advantage of direct control of boundary mobility. Other topological approaches include vertex or network, moving finite element, level set, computer Avrami, and neural network models [4].

Modeling challenges to be addressed in mesoscale approaches to recrystallization are abound. For example, realistic input data such as deformation structures, boundary properties, and constitutive descriptions are in general lacking. Deformed microstructure heterogeneity requires modeling features that are very small relative to the structure scale (~ 100 nm), such as local and nonlocal dislocation interactions, for accurate evaluation of local variation in the stored energy, which is still missing. Inadequate representation of some underlying physical processes is another example. i.e., a physics-based model for recrystallization nucleation is absent. As such, empirical rules are usually used for nucleation and simplifying assumptions about recovery are dictated. This leads to the fact that most recrystallization models are basically growth models. Moreover, the strong dependence of nuclei survival and growth propensity on their instantaneous location relative to the grain boundaries poses yet another modeling difficulty. The adequate accountability of these issues controlling nucleation and growth is critical for realistic representation of the heterogeneous aspect of this phenomenon. Capturing crystallographic texture, anisotropy in grain boundary properties (e.g., mobility and energy), and local misorientations of sub-grains represent additional levels of complexity to mesoscopic models. To overcome some of these challenges, a robust algorithm to construct deformation microstructure based on realistic data is needed. This is essential to determine the potential of preexisting embryos to transform into recrystallization nucleus and eventually form a new grain.

Advanced experimental techniques have been used extensively to investigate deformation microstructure in metals [9,37–43], which demonstrated the key role played by dislocations in the

structural evolution leading to grain subdivision. Dislocation substructure evolution is driven by two processes, dislocation multiplication followed by dynamic recovery. This eventually leads to formation of dislocation cell structure via dislocations rearrangement into dislocation walls with small fraction forming a Frank network in the cell [37]. Cell structure is characterized by two different types of dislocation boundaries with distinct attributes, namely, geometrically necessary boundaries (GNBs) and incidental dislocation boundaries (IDBs) [6,37]. Figure 1 illustrates sketches of typical deformation microstructure observed in a medium-high stacking fault energy metal for strain values below 1 (Fig. 1a) and larger than 2 (Fig. 1b) [44]. As strain increases, planar GNBs spacing and the cell size decrease and IDBs become relatively straight. These characteristics of microstructure refinement are observed at high strains. Figure 1c shows a typical distribution of the elastic energy density in deformed copper at a small strain determined using continuum dislocation dynamics (CDD), with the geometrically necessary dislocations (GND) density overlayed on the energy map [45]. CDD is becoming more predictive of the deformation microstructure as well as the elastic strain field of the dislocation system, hence the elastic energy. It can shed light on the energy density distribution in the system in connection with the dislocation patterns. Figure 1c also shows that the magnitude of the elastic energy is not negligible in the cell. This indicates the importance of accounting for the background energy distribution in the cell along with the dislocation core energy stored in the boundaries themselves. Furthermore, experimental evidence demonstrated the complex morphological evolution of the recrystallization front with local protrusions/retrusions adding a driving force for recrystallization comparable in magnitude to the stored energy contribution [39,42,43,46]. This causes the migration of recrystallization boundaries to exhibit stop-go behavior and kinetics that deviate significantly from classical models' prediction, which depend on averaged measures for stored energy and recrystallization boundary velocity.

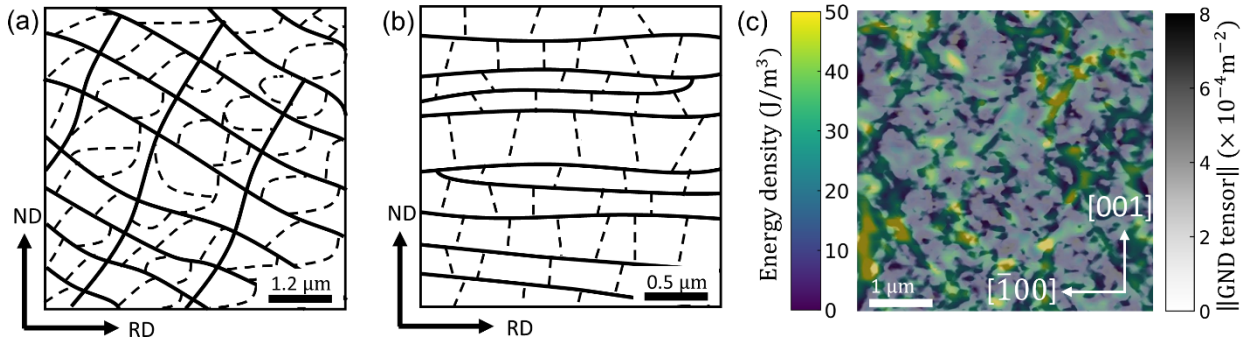

Fig. 1. Dislocation structure and distribution of elastic energy density in a rolled medium-high stacking fault energy metals. (a) At small strains (< 1) and (b) at large strains (> 2) [44]. (c) A continuum dislocation dynamics simulation result for a [001] tensile-loaded copper crystal at 1% strain viewed on (010) plane, showing the elastic energy being primarily concentrated near the GND walls followed by small packets of energy concentrated in the cells formed by the dislocations [45]. In (a) and (b), dashed and solid lines represent IDB and GNB, respectively.

Inspired by available detailed structural analysis of deformation microstructure observed experimentally and CDD findings, the current study presents a novel phase-field model for static recrystallization of plastically deformed metals accounting for deformation-energy field heterogeneity. Unlike previous works [46,47], the present model is the first-of-its-kind to incorporate realistic deformed microstructure by employing a statistical approach to represent local variation in the deformation-energy field due to dislocation cell structure using universal scaling laws and similitude relations [13,14]. The primary goal is to investigate the ability of this subgrain structure-informed model to reproduce the morphological evolution of recrystallization front with the experimentally observed protrusions/retrusions and investigate the impact of local variation in deformation field on recrystallization kinetics and final grain structure. The description of the stored energy field takes into consideration cell's interior energy variation. The effects of strain level and temperature are also investigated and the sensitivity of the model predictions to the statistical parameters representing the deformation-energy field is examined. The rest of the paper is organized as follows. The developed dislocation microstructure-informed model will be detailed

in Sec. 2. The phase-field method for recrystallization modelling will be discussed in Sec. 3. The results are presented and discussed in Sec. 4, followed by the summary and outlook in Sec. 5.

2. Dislocation Microstructure-Informed Recrystallization Model

2.1. Plastic deformation structures in metals

When grain subdivision is accompanied by easy three-dimensional mobility of dislocations via cross slip, dislocation cell structure is observed, which involves the formation of rotated volume elements [7,8,48]. The basic unit in this microstructure is the cell block, with long and nearly planar dislocation walls lying on special planes (GNBs) delineating these elongated cell blocks. Every cell block consists of approximately equiaxed cells, and each of these cells is bounded by short boundaries (IDBs). The dislocation density in the interior of these cells is much lower than the average dislocation density in the deformed matrix. Being formed by different mechanisms, cell block boundaries and cell boundaries have different characteristics [7,8,48]. GNBs accommodate the difference between macroscopic strain and cell block strain caused by slip pattern, so angular misorientations are controlled by the difference in glide-induced lattice rotations in the adjoining volume. At small strains, GNBs appear as dense dislocation walls, while at large strains, a single, nearly planar boundary enclosing a narrow cell block forms what is known as lamellar boundary (LB). On the other hand, IDB is a dislocation boundary formed by the mutual and statistical trapping of glide dislocations and supplemented by forest dislocations. At large strains, a Bamboo incidental dislocation boundary is observed, which is connected to GNBs (i.e., LBs) at the two ends. It separates two nearly empty volumes that are rotated from each other. The combination of lamellar and Bamboo boundaries together comprises the so-called lamellar structure. For the sake of demonstrating ideas, the present investigation will primarily focus on the lamellar structure.

Microstructural analysis using available TEM and EBSD data has been used to quantitatively describe the deformed state in terms of microstructural parameters [13,14]. Important microstructural parameters include boundary type, crystal orientation with respect to deformation axes, boundary plane, spacing, misorientation angle, and width. Cottrell was the first to suggest the relation between the local misorientation angle and recrystallization nucleation propensity [2]. Later, extensive experimental evidence supported his idea that nucleation occurs only at regions in microstructure with high local misorientation [7,8,48–55]. Although average dislocation boundaries spacing and average misorientation angle across them are continuously changing with strain, a scaling law has been observed for each boundary type independently. A universal probability distribution function can be used to represent the spatial distribution of these parameters in FCC metals. The scaling behavior applies when the universal function is normalized by the average value of the microstructural parameter for a given deformed state, which is usually determined using the equivalent von Mises strain (ε). Rayleigh distribution is used to express this universal function. For example, the probability distribution function of misorientation angle θ for a given average misorientation angle $\overline{\theta}(\varepsilon)$ across specific boundary type (i.e., GNB or IDB) is given by [16]

$$f\left(\frac{\theta}{\overline{\theta}}\right) = \frac{\pi}{2}\left(\frac{\theta}{\overline{\theta}}\right)\exp\left(-\frac{\pi}{4}\left(\frac{\theta}{\overline{\theta}}\right)^2\right). \quad (1)$$

Similarly, the probability distribution function of boundary spacing D for each of the two boundary types at a given average spacing $\overline{D}(\varepsilon)$ is given by

$$f\left(\frac{D}{\overline{D}}\right) = \frac{\pi}{2}\left(\frac{D}{\overline{D}}\right)\exp\left(-\frac{\pi}{4}\left(\frac{D}{\overline{D}}\right)^2\right). \quad (2)$$

From the microstructural analysis of GNBs and IDBs data, similar trends were found such as decrease (increase) of the average spacing (misorientation angle) with increasing the equivalent

strain. However, GNBs and IDBs exhibit some different characteristic behaviors. For example, the average misorientation angle across GNBs $\left(\overline{\theta}_{\mathrm{GNB}}\right)$ does not saturates with higher strain, in contrast to IDBs, i.e., $\left(\overline{\theta}_{\mathrm{IDB}}\right)$. Furthermore, misorientation angle distribution of GNBs does not necessarily follow the scaling law at high strains [7,48]. Two similitude relations were also observed for microstructural parameters [48]. The first gives the interrelationship between boundary spacing (D), misorientation angle (θ), and Burgers vector (b). It takes the form

$$\frac{D\theta}{b} = C, \tag{3}$$

where C is a constant. The second gives the relation between dislocation wall thickness (w) and GNBs average spacing

$$w = f_{\mathrm{w}}\overline{D}_{\mathrm{GNB}}. \tag{4}$$

In this relation, f_{w} is a small fraction. To construct the lamellar structure, typical experimental values for this fraction [7,48] will be used in the developed model to fix individual boundaries width in terms of average spacing. This relation will be also assumed true for IDBs.

2.2. Deformation energy representation & lamellar structure construction algorithm

Driven by energy minimization, the tangled dislocations tend to rearrange themselves in certain patterns. Theoretically, these rearrangements can be interpreted in the context of the theory of Low Energy Dislocation Structures (LEDS). In LEDS theory, the assumption of elastic distortion being restricted to a region close to the boundary [14–16] leads, in the absence of long-range stresses, to Frank's formula for the relationship between dislocation content of a boundary and its angle axis pair (**R**/θ) [7]. Burgers vectors net content, **B**, in small angle boundary is given by [7]

$$\mathbf{B} = (\mathbf{r} \times \mathbf{R})2\sin\left(\frac{\theta}{2}\right) \tag{5}$$

where, **r** is a vector lying in the boundary containing dislocations network and intersecting them all. The low-energy structures assumption also leads to Read-Shockley equation for the relation between elastic energy per unit area of the boundary, E_{a}, and the misorientation angle [16]

$$E_{\mathrm{a}} = \begin{cases} \gamma_{\mathrm{m}}\left(\frac{\theta}{\theta_{\max}}\right)\left(1 - \ln\left(\frac{\theta}{\theta_{\max}}\right)\right), & \theta \leq \theta_{\max} \\ \gamma_{\mathrm{m}}, & \theta > \theta_{\max} \end{cases}. \tag{6}$$

In the above, γ_{m} is the high angle-grain boundary energy, which is independent of misorientation angle. Here, $\theta_{\max}$ for a low-angle boundary is taken as 15°. Scaling laws, similitude relations, and Read-Shockley equations are used here to create a realization of the deformation-energy field associated with lamellar structure. Typical values for FCC metals are used to parametrize the algorithm, which is used as initial configuration in recrystallization model. Lamellar structure is represented in 2-D. Nevertheless, extending the algorithm to 3-D is straightforward. Cell blocks are created using horizontal GNBs extended over the entire domain. GNBs spacing is randomly sampled from Rayleigh distribution, i.e.,

$$\frac{D}{\overline{\overline{D}}} = \sqrt{-\left(\frac{4}{\pi}\right)\ln(1-u)}, \tag{7}$$

with u being a pseudo-random number sampled from a uniform distribution defined on the period [0, 1]. To constrain sampled boundary spacing values within the range employed in the microstructural analysis, $\frac{1}{3} \leq \frac{D}{\overline{\overline{D}}} \leq 3$ inequality is imposed. Similarly, spacing between contiguous IDBs belonging to the same cell block is sampled from Rayleigh distribution. IDBs are represented by straight lines that are inclined at an angle from the domain vertical axis and randomly chosen from arbitrary range: $15° - 35°$. Successive IDBs in each cell block tilt in alternate directions and bridges only two LBs, i.e., do not extend beyond cell block boundary. For smaller von Mises strains (< 1), IDBs curvature is represented using a parabola equation.

The misorientation angle across each dislocation boundary is chosen such that the first similitude relation, Eq. (3), holds true. Accordingly, the deformation-energy field at any point with Cartesian coordinates (x, y) in deformed matrix takes the form

$$f_{\mathrm{def}}(x,y) = \sum_{i=1}^{N_{\mathrm{GNB}}} \sum_{j=1}^{N_{\mathrm{IDB}}} \max\left(E_{\mathrm{a},i}\delta(y-y_i), E_{\mathrm{a},j}\delta\left(\left|r_{\perp,j}(x,y)\right|\right)\right) + C_{\mathrm{cell}} \qquad (8)$$

In Eq. (8), total number of GNBs and IDBs are labelled by N_{GNB} and N_{IDB}, respectively. The energy per unit area of the ith GNB (defined by the equation: $y = y_i$) and the jth IDB are denoted by $E_{\mathrm{a},i}$ and $E_{\mathrm{a},j}$, respectively. The deformation-energy consists of two terms, the first is attributed to lamellar structure, while the second, C_{cell}, represents the elastic energy stored in individual cells interior and is assumed to be constant within each cell. Inspired by CDD results, the value of this constant varies from one cell to another depending on the individual cell area. Assuming inverse proportionality between the cell area and the elastic energy density, the smallest and the largest cells in the domain are assigned the highest and the lowest values for the deformation-energy density, respectively. Linear interpolation is then used to determine the magnitude of C_{cell} for all other cells. In addition to zero value for this constant, three different ranges for cell's interior energy density are considered, which were chosen to be a fraction of the highest sampled GNB deformation-energy density. Using Eq. (6), the energy per unit area of each boundary is calculated in terms of its misorientation angle. The truncated distribution functions $\delta(y-y_i)$ and $\delta\left(\left|r_{\perp,j}(x,y)\right|\right)$ represent energy smearing across the dislocation boundary width for GNBs and IDBs, respectively, with contours taken to be parallel to the corresponding dislocation boundary, e.g., $\left|r_{\perp,j}(x,y)\right|$ is the normal distance between the point and the corresponding IDB. To keep deformation-energy localized about dislocation boundaries, the smearing factor is set to one half of the boundary width $\left(\frac{w_i}{2}\right)$. In addition, GNBs screen the stress field associated with IDBs, so

IDBs distribution function is set to zero for points outside the same cell block. In this regard, the role of the maximum function appearing in the expression is to handle the special situation where the point lies close to the corner of the dislocation cell with possible contribution from both the nearby GNB and IDB. Unit pulse function is employed to represent the distribution function in the present study. It takes the form

$$\delta(y - y_i) = \begin{cases} \frac{1}{w_i}, \text{if } |y - y_i| \leq \frac{w_i}{2} \\ 0, \text{otherwise} \end{cases}. \quad (9)$$

For comparison, Gaussian distribution is also examined. The lamellar structure model is parameterized for two different strain levels listed in Table 1 [7].

Table 1. Average microstructural parameters for lamellar structure model.

Parameter	ε	$\overline{\boldsymbol{D}}_{\mathbf{GNB}}(\boldsymbol{\varepsilon})$ [μm]	$\overline{\boldsymbol{D}}_{\mathbf{IDB}}(\boldsymbol{\varepsilon})$ [μm]	$\overline{\boldsymbol{\theta}}_{\mathbf{GNB}}(\boldsymbol{\varepsilon})$	$\overline{\boldsymbol{\theta}}_{\mathbf{IDB}}(\boldsymbol{\varepsilon})$	$\boldsymbol{f}_{\mathbf{w}}$
State 1	2.5	0.20	0.4	13.8°	2.6°	0.04
State 2	4.5	0.16	0.3	19.5°	3.0°	0.04

3. Phase-Field Modeling of Recrystallization

The phase-field method is a versatile mathematical tool for studying interfacial evolution in materials. Its flexibility makes it powerful in tracking quantitatively the coevolution of the microstructure and properties of the dynamic system, while consistently imposing thermodynamics constrains on the kinetics of the problem [4,25–27]. Several researchers employed phase-field to model recrystallization [4,29–34,46,47]. Following Landau's approach, Moelans et al. [27–30] developed a model for grain growth that can account phenomenologically for anisotropic grain boundary properties, assuming constant molar volume and thermal equilibrium. This grain growth model was used to study the recrystallization of isotropic system [29]. For this purpose, the different terms of the free energy density, see Eq. (15), were formulated as

$$f_{\text{local}} = \frac{6\sigma_{\text{gb}}}{l_{\text{gb}}}\left[\sum_{i=1}^{N}\left(\frac{\eta_i^4}{4} - \frac{\eta_i^2}{2}\right) + \frac{3}{2}\sum_{i=1}^{N}\sum_{j=1}^{N}\eta_i^2\eta_j^2 + \frac{1}{4}\right], \tag{10}$$

$$f_{\text{gradient}} = \frac{3}{8}\sigma_{\text{gb}} l_{\text{gb}} \sum_{i=1}^{N}(\nabla\eta_i)^2, \tag{11}$$

$$f_{\text{stored}} = f_{\text{def}}(x, y)\rho_{\text{eff}}(\eta_1, \eta_2, \ldots, \eta_N). \tag{12}$$

Respectively, the above are the local or multi-well energy, gradient energy, and the stored energy density. The former two components are associated with the boundaries between the nuclei and the deformed matrix, with the latter carrying the stored energy. Here, $\eta_1, \eta_2, \ldots, \eta_N$ are order parameters representing nuclei embedded in the matrix, while the order parameter η_0 represents the deformed matrix. The order parameter, for example, η_1 equals 1 in the nuclei 1, while all other fields equal 0. At the grain boundaries, all the fields smoothly vary between their equilibrium values in the adjacent grains. σ_{gb} and l_{gb} are the model parameters representing the grain boundary energy and diffuse interface width, respectively. An analytical function $f_{\text{def}}(x, y)$ was used in Eq. (12) to represent the deformation-energy field in the matrix multiplied by an interpolating function $\rho_{\text{eff}}(\eta_1, \eta_2, \ldots, \eta_N)$ ensuring smooth variation of the deformation energy from the background matrix values to zero in the nuclei. A proper account of the mechanics of the medium shows that zero deformation energy density in the nuclei is an approximation worth further investigation. The interpolation function, named local deformation fraction, is given by

$$\rho_{\text{eff}}(\eta_1, \eta_2, \ldots, \eta_N) = \frac{\sum_{i=1}^{N}\eta_i^2 \mathrm{I}_{Def}(i)}{\sum_{j=1}^{N}\eta_j^2}, \mathrm{I}_{Def}(i) = \begin{cases} 1, & i \in Def \\ 0, & \text{otherwise} \end{cases}, \tag{13}$$

where *Def* denotes the set of deformed grain indices. Using a single value for nuclei boundary mobility M, the time-dependent Ginzburg–Landau equations of the order parameters take on the form

$$\frac{\partial \eta_i}{\partial t} = -\frac{4}{3}\left(\frac{M}{l_{\text{gb}}}\right)\left(\frac{\delta F}{\delta \eta_i}\right), \tag{14}$$

where F is the free energy functional given by the integral of the three energy components discussed earlier over the materials volume,

$$F = \int \left(f_{\text{local}} + f_{\text{gradient}} + f_{\text{stored}}\right) dV. \tag{15}$$

Moelans et al. [29] applied their model on a 2-D system consisting of a single grain representing the deformed matrix and a single grain representing the recrystallized grain. Isotropic values for model parameters were taken from experiments for Ni and Al. The grain boundary was assumed to be initially planar, and the migration of the boundary was studied in one direction only, while periodic boundary conditions was assumed in the other direction. The main goal of the study was to investigate the impact of the local variation of deformation energy field on the local migration of recrystallization boundary in deformed metals. For this purpose, three different forms of sinusoidal function were tested, and the morphology of the recrystallization front was analyzed. The study clearly showed the sensitivity of the morphology of recrystallization boundary to the local variation of the deformation-energy over its course of evolution, which introduced regions of protrusions and extrusions to the originally flat boundary. A subsequent study was conducted by the same authors [30] that allowed a two-dimensional variation in the deformation energy, which lead to the development of a more complex morphology of the recrystallization front. Although the results obtained from these studies agree with experimental observations, the use of analytical functions to represent deformation-energy field (instead of considering realistic description) renders the agreement qualitative and of theoretical interest.

Very recently, Yadav et al. [46,47] used an idealized deformed structure comprising different sets of GNBs to study the effect of the heterogeneous deformed microstructure on the migration of the recrystallization front into the deformed region and its morphology. In one study, the authors varied the spacings between the GNBs, while keeping the average stored energy constant. In another study, they examined the effect of geometric alignment of two sets of intersecting GNBs with respect to the flat recrystallization front, corresponding to low strain, on the morphology of the recrystallization front and the average velocity. They also used a single set of parallel GNBs to represent the deformed structure for a high strain scenario. Yadav et al. [46] elucidated the anisotropic migration of different segments of a recrystallized nucleus in the deformed microstructure by varying the alignment of the GNBs in front of the flat recrystallization boundary. Stop and go motion of the recrystallization front boundaries was observed in the simulations, and the results revealed that the morphology of the recrystallization front and the velocity strongly depend on the deformed microstructure. It was also reported [47] that the roughness of the recrystallization front and its average velocity increased with the increase in the spacing between the GNBs and the stored energy. However, the average velocity increase with the increase in spacing implies that the migration velocity is faster in low strain scenarios, which contradicts experiment. This discrepancy could be attributed to the inadequate treatment of GNB spacing and the stored energy as two independent parameters and the lack of accountability to the variation in the deformation-energy across different GNBs (by using average stored energy). IDBs were not considered in these studies.

Gentry and Thornton [31] modified Moelan's model to parametrize a phenomenological model of static recrystallization of plastically deformed commercially pure titanium. The simulated kinetics of recrystallization were used to parameterize the Avrami equation

$$X = 1 - \exp\left(-\beta\left(\frac{t}{t_{0.5}}\right)^{n}\right), \tag{16}$$

which yields the fraction of the recrystallized volume X as a function of the annealing time. In this equation, $\beta = \ln 0.5$, n is the time exponent, and $t_{0.5}$ is the time required for the recrystallization fraction to reach the value of 0.5. Experimental data for commercially pure titanium compressed by 20% at room temperature and annealed at a temperature of 800 °C were used for Moelan's model parametrization. In addition, the deformation-energy was defined as the dislocation core energy, and described in terms of the shear modulus, the Burgers vector, and the grain-averaged dislocation density. In that study, initial recrystallized nuclei were added at the beginning of simulation to model static recrystallization of polycrystals in 2-D and assumed to be dislocation-free.

The impact of deformation mode on recrystallization kinetics and microstructural evolution was investigated by Athreya et al [32]. This study employed both experimental and computational techniques. For this purpose, materials subjected to the same equivalent plastic strain were deformed by torsion and rolling. The phase-field approach was used to study the recrystallization kinetics of the highly deformed matrix through the growth of preexisting strain-free nuclei. A multi-phase field model was used to simulate the coarsening of the grains driven by the stored energy as well as the grain boundary curvature. Since phase-field mobility parameters should be supplemented as an input, a mean field model for recrystallization, which assumes the strain-free nuclei growing in a uniform stored-energy field (taken to be time dependent) was utilized to extract these parameters from experiment for different deformation structures. Instead of using the potential well with multiple degenerate minima along with an explicit term for the stored energy (as in Moelan's model), they used a multi-well potential with unequal heights/depths for this purpose. The unequal heights/depths is supposed to capture the stored energy differences between

the grains. Although the study used a mean field parameter, it succeeded to capture the sensitivity of recrystallization kinetics to the local variation of the deformation structure, by considering the impact of the deformed state on the mobility.

In all the above models, the contribution of the non-local term of the long-range dislocation strain field to the elastic energy density was never considered. Sreekala and Haataja [33] developed a dislocation density model coupled to the phase-field method to simulate the growth of an isolated recrystallized grain (within a cold-worked matrix) in 2-D. Dislocation long-range interactions were modeled based on linear elasticity theory, using a coarse-grained dislocation density description (continuous Burgers vector field). In addition, the short-range (core) interactions are accounted for using constitutive relations for local dislocation reactions. As before, the initialization assumed a recovered state with nuclei formed (recovery stage is not considered) and isotropic medium (grain boundary). Moreover, the average dislocation density was kept constant during the simulations, but different idealized dislocation structures were tested. In Sreekala and Haataja [33], the relation between the strain and the stress tensors was developed using the mechanical equilibrium equations, within linear elasticity framework, by applying the closure failure relation. The elastic energy was derived in terms of the Airy stress function. Abrivard et al [56,57] developed a coupled phase-field and crystal plasticity framework to study different aspects of static and dynamic recrystallization. In that study, high stacking fault energy material was considered to investigate the role played by the strain induced boundary migration. However, the effect of the grain dislocations substructures was absent.

4. Numerical Scheme, Results and Discussion

The recrystallization model developed here is used to study the temporal evolution of the morphology of recrystallization front for several recrystallization nuclei embedded in a deformed

matrix with a size equivalent to a single grain. Recrystallization kinetics are assessed in terms of the fitting parameters of the Avrami equation. In addition, the influence of the relative location of recrystallization nuclei embryo with respect to dislocation walls on the grain structure after the completion of the primary recrystallization stage and consequently on the surviving grains over the course of grain coarsening (which determines the final texture) is discussed. Moreover, the effect of several deformed state parameters on recrystallization kinetics are analyzed. This includes the amount of mechanical/deformation work (via average boundary spacing and misorientation angles at a given von Mises strain) and temperature (via grain boundary mobility). Furthermore, the sensitivity of the results to different mathematical representations of the heterogeneous deformation-energy field is investigated. For example, the impact of the statistical distribution used in the sampling of the dislocation wall spacing is assessed by comparing the results for a Rayleigh (R) distribution with those corresponding to an equispaced (E) distribution. Moreover, the effect of two different energy smearing methods across the dislocation boundaries, namely, unit pulse (U) and Gaussian distribution (G) is also studied. Finally, the influence of the background energy inside the dislocation cell on the observed dynamics is also analyzed by considering four different cases represented by different ranges in terms of the highest possible GNB energy density, with the first being zero energy and the rest have the following ranges: 0.5%-1.5%, 2.5%-7.5%, and 5%-15%. This corresponds to four different levels, namely, zero (Z), low (L), medium (M), and high (H), respectively. For convenience, the deformation-energy field associated with different variants of the parameters is labelled using a quadruple index notation. From the leftmost index, the first index stands for the statistical distribution used in the random sampling (R or E), the second index signifies the strain level ($\varepsilon_{2.5}$ or $\varepsilon_{4.5}$), the third index labels the used energy smearing method (U or G), and the fourth index labels the level of energy assigned to the interiors of cells (Z, L, M, or H). For example, the deformation-energy field referenced

by $R\varepsilon_{2.5}UZ$ is constructed using the Rayleigh distribution for the sampling of GNB and IDB spacing corresponding to a von Mises strain of 2.5 with the energy across the boundaries smeared according to the unit pulse function and no deformation-energy assigned to the cells. Since by model construction the initial deformation-energy field is independent of grain boundary mobility, this variable is reported separately and not included in the indicial notation. Unless stated otherwise, grain boundary mobility is selected to be 2×10^{-12} m^4/J·s.

Table 2. Model parameters.

Parameter	$\boldsymbol{\sigma_{gb}}$ [J/m^2]	$\boldsymbol{M}$ [m^4/J.s]	$\boldsymbol{l_{gb}}$[nm]
Value	0.8	2×10^{-13}, 2×10^{-12}	40

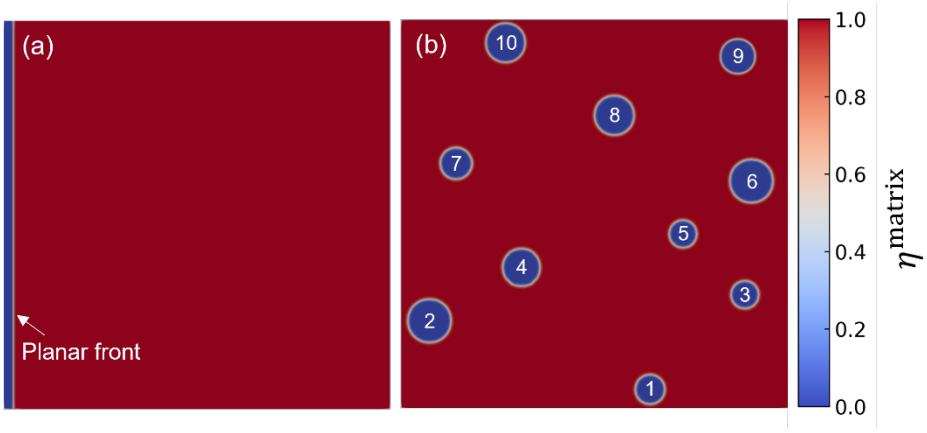

Fig. 2 Initial configurations. (a) Planar recrystallized front initialized at $x = 10$ in a 4×4 micron 2-D deformed matrix. (b) Initial arrangement of the 10 recrystallized nuclei embryos in a 4×4 micron 2-D deformed matrix. The nuclei vary in size and are indexed in the order of increasing y-coordinate. The radius of the embryos, arranged in an ascending order according to their index, is as follows: 1→150 nm; 2→220 nm; 3→140 nm; 4→190 nm; 5→140 nm; 6→220 nm; 7→160 nm; 8→200 nm; 9→170 nm; and 10→210 nm.

4.1. Numerical scheme and model parameters

The phase-field model used in the present study employs Eqs. (10)-(12) to calculate the free energy density and assumes isotropic properties for the grain growth. Table 2 lists all model parameters. The heterogenous deformation-energy field is represented by Eq. (8). To track the kinetics of the

388 system, the Allen-Cahn equation, Eq. (14), is solved using the Finite Element Method (FEM).
389 Specifically, the continuous Galerkin method is invoked via the phase-field module available in
390 the simulation package MOOSE framework [58]. Moreover, the Preconditioned Jacobian-Free
391 Newton-Krylov method (PJFNK) was sought for solving the formed nonlinear equation system of
392 the weighted residuals. A new object was implemented within MOOSE to incorporate the lamellar
393 structure as an initial configuration for the deformation-energy field description in the deformed
394 matrix, according to Sec. 2.2. Adaptive timesteps with a maximum size of 2 ms were used. The 2-
395 D deformed matrix is taken to be a square with initially small, circular recrystallized nuclei
396 embryos embedded into it. In all simulations, the recrystallized nuclei embryos are assumed to be
397 dislocation-free with zero stored energy. A square mesh (QUAD4 elements) was utilized to
398 discretize the spatial domain, with the mesh spacing set to 5 nm. The deformed matrix size was set
399 to 4 μm × 4 μm in all simulations. In this study, we selected two initial configurations for the
400 recrystallized nuclei to understand the morphology evolution of the front and kinetics of the
401 recrystallization phenomena under varied heterogeneous deformation-energy fields. Figure 2(a)
402 shows a planar recrystallization front initialized at $x = 10$ which is supposed to capture the front
403 evolution of a large nuclei. Dirichlet boundary conditions are assumed for the fields along X-axis,
404 while periodic boundary conditions along Y-axis. Figure 2(b) shows the initial configuration of
405 the seeded recrystallized nuclei embryos embedded in the 2-D deformed matrix, with each embryo
406 assigned a unique order parameter and a certain radius within the range 140–220 nm. The nuclei
407 are arranged in the domain such that their centers are separated by at least 800 nm. Periodic
408 boundary conditions were imposed for the latter configuration. For the sake of comparison,
409 classical nucleation theory is utilized to calculate the critical radius r_{crit} in terms of the average
410 deformation-energy density of the deformed matrix $\bar{f}_{\mathrm{def}}$ and the surface energy per unit area σ_{gb},
411 using the relation

$$r_{\text{crit}} = \frac{\sigma_{\text{gb}}}{\bar{f}_{\text{def}}}. \tag{17}$$

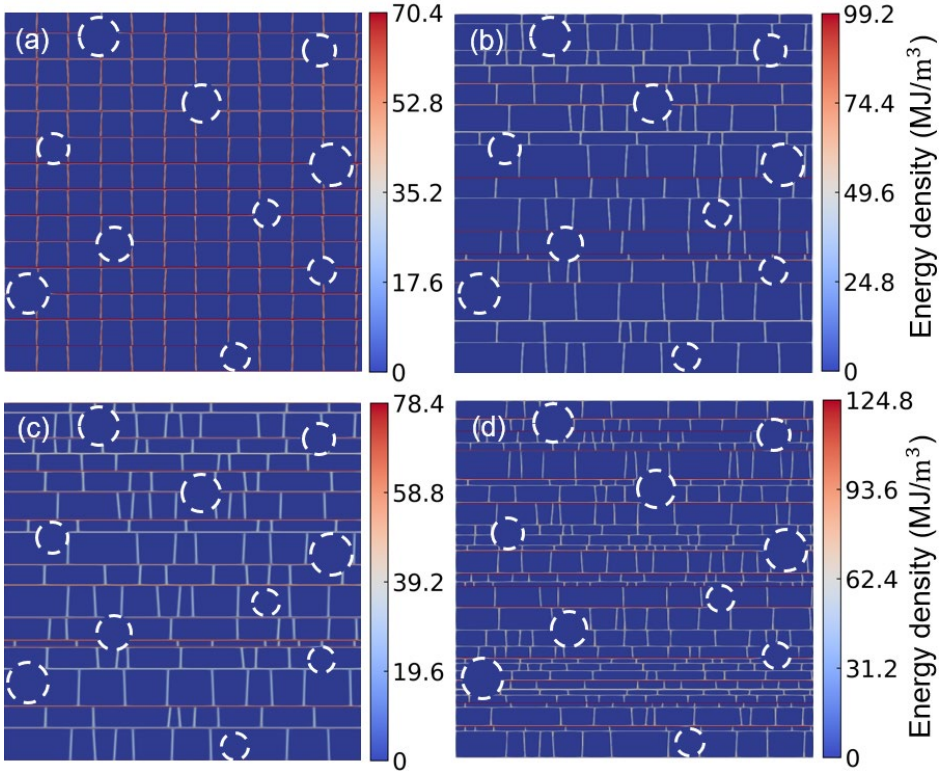

Fig. 3. Different deformation-energy density fields chosen for the study in a 4×4 micron domain. The white circles outline the boundary of the nuclei shown in Fig. 2(b). The horizontal lines represent the GNBs, and the vertical lines represent IDBs. The cell enclosed by the GNBs and IDBs is undeformed with zero energy density. (a) Equispaced IDBs and GNBs at $\varepsilon = 2.5$ with boundary energy distributed evenly across the interface width using a unit pulse function ($\text{E}\varepsilon_{2.5}\text{UZ}$). (b-c) Rayleigh distribution sampled spacing for IDBs and GNBs at $\varepsilon = 2.5$ with boundary energy across the interface width sampled from statistical distribution using (b) a unit pulse function and (c) a gaussian function, i.e., $\text{R}\varepsilon_{2.5}\text{UZ}$ and $\text{R}\varepsilon_{2.5}\text{GZ}$, respectively. (d) Rayleigh distribution sampled spacing for IDBs and GNBs at $\varepsilon = 4.5$ with a unit pulse function used to assign boundary energy across the interface width ($\text{R}\varepsilon_{4.5}\text{UZ}$). The average deformation-energy density in cases (a), (b) and (c) is kept fixed at around 4.63 MJ/m^3, and in case (d) at 7.7 MJ/m^3.

The values for the different levels of cell's interior energy assignment are reported in Table 3 along with the relevant domain-averaged parameters. From this comparison, it is obvious that classical nucleation theory predicts the largest seeded recrystallization nuclei embryos to grow in all cases, while the smallest ones shrink and disappear in the two lowest levels for cell's interior energy. i.e., the selected range for recrystallization nuclei radius is about the critical radius. Figures 3 and 4 illustrate the initial deformation-energy field associated with the different simulated cases

(as indicated in the caption of each figure). As highlighted earlier, all simulations consider solely static recrystallization under the assumptions that neither recovery processes nor deformation-energy relaxation (within the deformed region) occurs during simulation time.

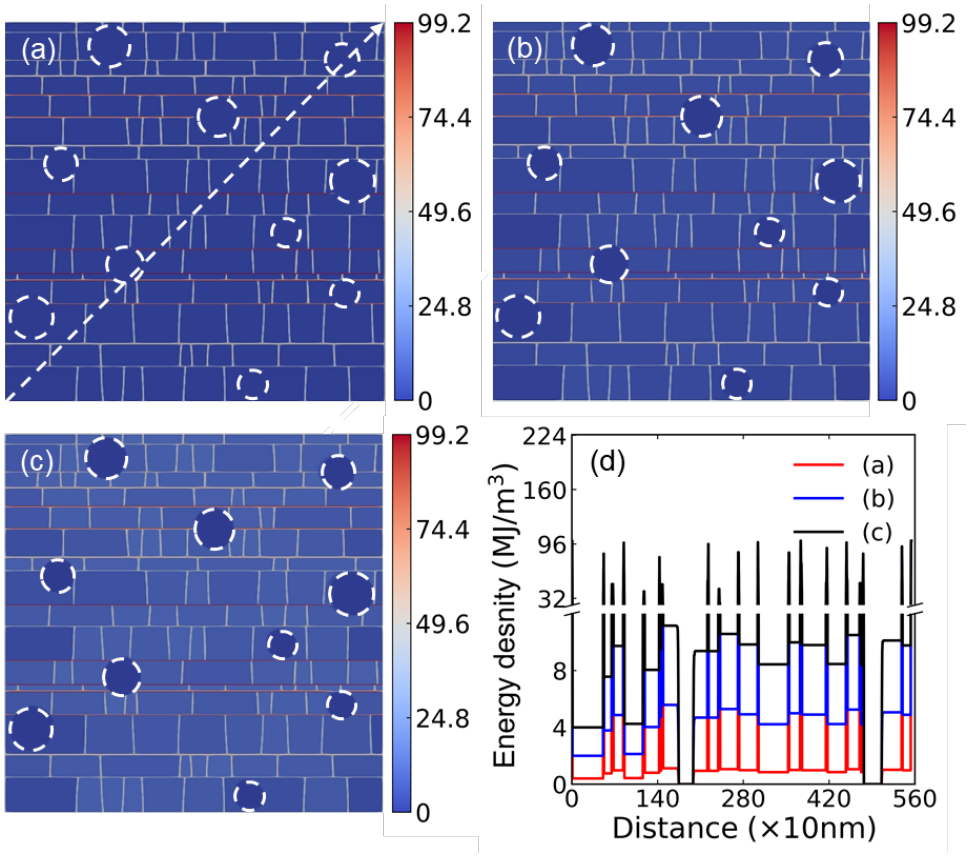

Fig. 4. Different cell energy distributions for a Rayleigh distributed spacing between the boundaries at $\varepsilon = 2.5$ in a 4×4 micron domain. The horizontal lines represent the GNBs, and the vertical lines represent IDBs. The magnitude of the energy density in the cell's interior is area dependent with the smallest cell assigned highest possible value and the largest cell with lowest possible value. The maximum and minimum energy densities of a cell is chosen to be a fraction of highest possible GNB energy density with the ranges being (a) 0.5%-1.5% ($R\varepsilon_{2.5}UL$), (b) 2.5%-7.5% ($R\varepsilon_{2.5}UM$), and (c) 5%-15% ($R\varepsilon_{2.5}UH$). (d) Line plot showing the variation of the energy density across the diagonal, as shown in (a), for the configurations (a-c).

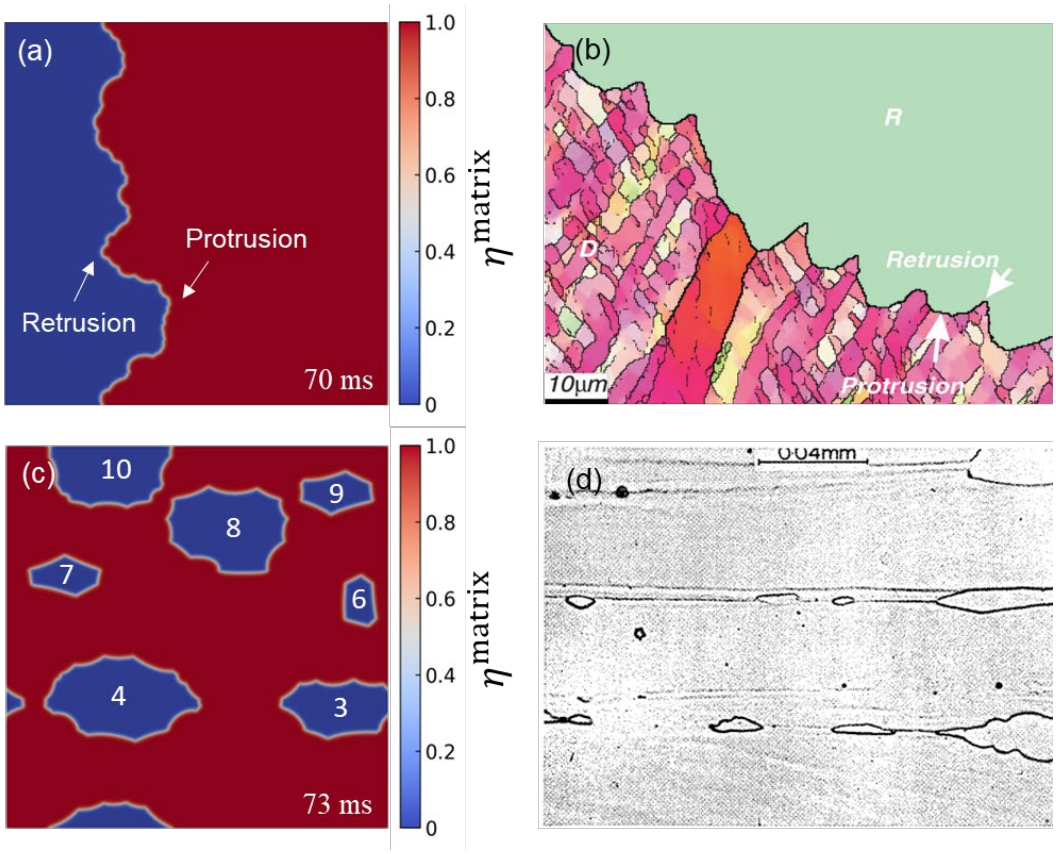

Fig. 5. Recrystallization front morphology. (a) Recrystallization front profile of a planar front growing into a deformed matrix for the deformation energy state R$\varepsilon_{4.5}$UZ. (b) Migrating recrystallized boundary formed in 50% cold rolled pure Al at room temperature, followed by annealing at 250 °C for 10 min, adopted from. [29]. (c) Recrystallization front profiles growing into a deformed matrix for the deformation energy state R$\varepsilon_{2.5}$UZ. (d) An optical micrograph showing the recrystallized nuclei growing along a transition band in a heavily rolled iron-3% silicon, followed by annealing at 600 °C for 25 min, adopted from [9].

Although the initial circular morphology of the recrystallized nuclei is not generally accurate, it is to be noted that this work is not primarily concerned with the nucleation mechanism of the recrystallization process but with capturing the morphological evolution of the recrystallization front in a realistic deformed microstructure using the phase-field modeling technique. However, since the microstructure development is very sensitive to the arrangement of dislocations, it is imperative to get the initial configuration accurate. There exist many possibilities in achieving the latter and one such approach involves generating the initial structures based on the microstructural images and another approach requires performing continuum dislocation dynamics simulations that gives the three-dimensional arrangement of the dislocations. However, as of now, the latter is

not adequately mature.

Table 3. Parameters characterizing the deformed state.

Deformed state	$R\varepsilon_{2.5}UZ$	$R\varepsilon_{2.5}UL$	$R\varepsilon_{2.5}UM$	$R\varepsilon_{2.5}UH$
$\overline{f}_{def}$(MJ/m^3)	4.63	5.42	8.55	12.43
Cell's interior energy contribution	0%	14.58%	45.85%	62.75%
Critical radius (nm)	173	148	94	64

4.2 Recrystallization front morphology and microstructure evolution

To observe the evolution of well-established recrystallization front, we initialized a planar front on the left side of a domain in the deformed state $R\varepsilon_{4.5}UZ$. Figure 5(a) shows the structure of the recrystallized front at time ~ 70 ms. The front was found to exhibit protrusions/retrusions configuration like was experimentally observed and shown in Fig. 5(b) [29]. The protrusion/retrusion configuration depends on the density of the boundaries ahead of the front and is rather a collective effect of many boundaries. By comparing the morphology of the recrystallized front with the deformation-energy field for the state $R\varepsilon_{4.5}UZ$, shown in Fig. 3(d), it is evident that the protrusions have formed in the regions where the density of boundaries was high relative to the neighboring regions, and retrusions formed in the regions where the density was low relative to its surroundings. As shown in Fig. 5(b), the experimental result supports this observation. Figure 5(c) shows the morphology of a number of recrystallized nuclei prior to impingement for the deformation energy state $R\varepsilon_{2.5}UZ$. The heterogeneous dislocation structure causes the appearance of the protrusion as a sharp cusp along the boundaries into the deformed matrix, while retrusion with a concave shape curved into the nuclei. Note that the morphology of the recrystallization front appears different at the two scales, i.e., Fig. 5(a) and Fig. 5(c), suggesting that the evolution of the front differs between small nuclei and well-established fronts. This difference is being captured here for the first time. The recrystallization front at the scale of a single cell protrudes along the dislocation boundary thus forming a relatively sharp cusp into the matrix at every single boundary.

At a larger scale, however, the average curvature can be quite the opposite in spite of the behavior at the individual boundaries. In addition, Fig. 5(c) shows the nuclei growing primarily along the GNBs as they are relatively high in energy density compared to IDBs, explaining the shape of the nuclei in Fig. 5(d).

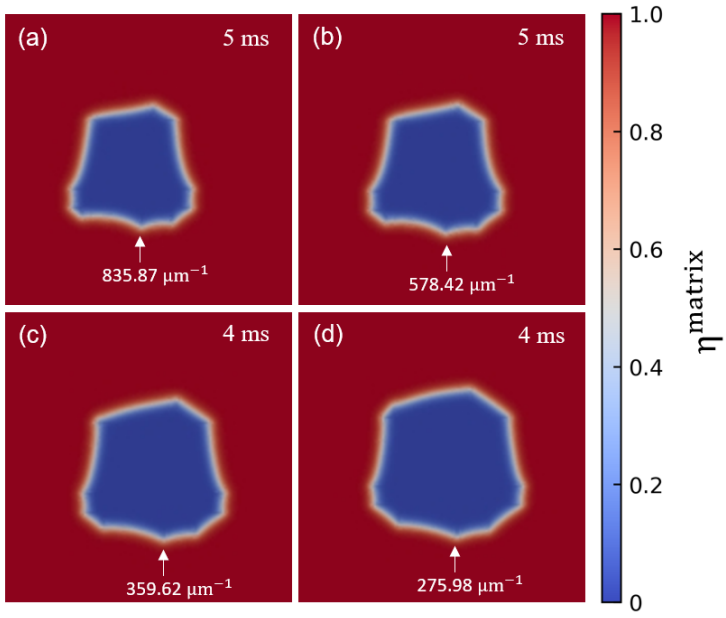

Fig. 6. Recrystallization front profile dependence on various energy distributions in the interiors of a cell for the nucleus #4. (a) $R\varepsilon_{2.5}UZ$, (b) $R\varepsilon_{2.5}UL$, (c) $R\varepsilon_{2.5}UM$, and (d) $R\varepsilon_{2.5}UH$.

To investigate the impact of the cell energy on the observed protrusions, Fig. 6 depicts the morphology of nuclei 4 early in time during the recrystallization stage for different levels of energy in the dislocation cell, namely, $R\varepsilon_{2.5}UZ$, $R\varepsilon_{2.5}UL$, $R\varepsilon_{2.5}UM$, and $R\varepsilon_{2.5}UH$. The initial boundary of this nucleus intersects with several IDBs and GNBs. It is evident that as the energy density in the cell increases, smoothing of protrusions takes place, i.e., reduction in curvature of the boundary line at the protrusion, as shown for the protrusion point marked with a white arrow in Figs. 6a-d. The improved mobility of the recrystallization front into the dislocation cell partially compensates for the preferential growth along the dislocation boundaries and lead to a reduction in the curvature at the protrusion. To quantitatively characterize this effect, the curvature at the marked point is

estimated for each case using the ImageJ software [59]. The curvature significantly decreased from 835.87 μm^{-1}, for the case with zero cell energy, to the value of 275.98 μm^{-1} when the cell-energy distribution belongs to the highest level considered.

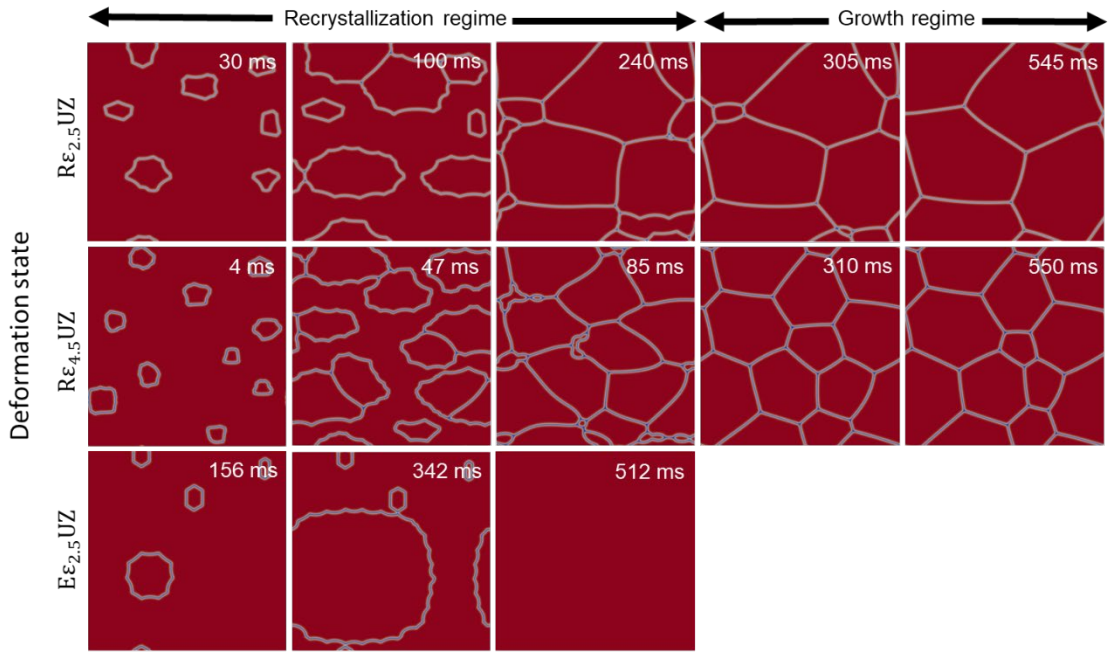

Fig. 7. Effects of the heterogeneity in the underlying deformed structure on the growth of nuclei in both recrystallization and grain coarsening stages. Rows from the top corresponds to deformation states $R\varepsilon_{2.5}UZ$, $R\varepsilon_{4.5}UZ$, and $E\varepsilon_{2.5}UZ$, respectively (see Fig. 3).

To better visualize the effect of deformation-energy field heterogeneity on the observed dynamics the evolution of individual recrystallization nuclei into the deformed matrix over the simulation time is tracked and the grain structure is analyzed. Snapshots of the microstructural evolution during recrystallization and grain coarsening stages at different times are displayed in Figs. 7 and 8 for different deformation-energy field configurations. There exist two types of boundaries: one between the recrystallized nuclei which is flat and the other being the recrystallization front of the nuclei with a non-smooth signature. Given the fact that the initial recrystallization nuclei configuration is identical, the considerable variation in the obtained final grain structure serves as evidence of the strong sensitivity of the recrystallization to local variation

in the deformation-energy field. For example, Fig. 7 shows how accounting for average deformation-energy density is not enough to capture the microstructural evolution, due to the high dependence on the arrangement of the dislocation walls.

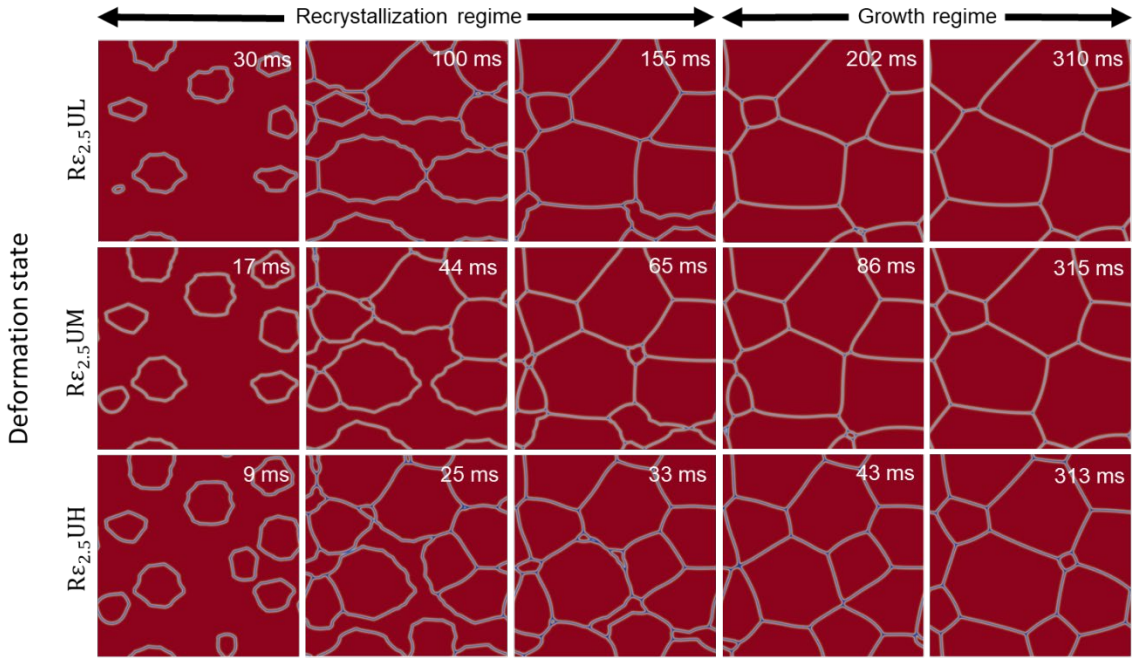

Fig. 8. Effects of varying deformation-energy density in the cells on the growth of nuclei in both recrystallization and grain coarsening stages. Each row, starting from the top, depicts the microstructure evolution when the cell is assigned an energy density value that fall in the range 0.5%–1.5%, 2.5%–7.5%, and 5%–15% of the highest GNB energy density in the domain. The corresponding deformation states are mentioned on the far-left side of each row (see Fig. 4).

Furthermore, Fig. 7 indicates that the use of the average dislocation boundary spacing to capture the heterogeneity of the deformation-energy field, as was done by Yadav et al. [47], is not sufficient for a reliable prediction of the microstructural evolution during the recrystallization. Accounting for the statistical variation in the dislocation boundary spacing is imperative. As would be expected, increasing the magnitude of deformation-energy density, by increasing the strain level (as in Fig. 7) or the cell energy level (as in Fig. 8), accelerates the kinetics and can result in a completely different microstructure development. For example, smaller nuclei like 1 and 5 (Fig. 2(b)) survive in the larger strain and highest cell-energy levels, whereas they shrink to zero size in

all the other scenarios. It is worth mentioning that faster kinetics was also obtained when the higher grain boundary mobility was used. However, due to the decoupling between the deformation-energy density and the grain boundary mobility, no effect on the final microstructure was observed.

4.3 Recrystallization kinetics

The sensitivity of the recrystallization model to various parameters characterizing the underlying heterogeneous deformation structure is assessed by comparing the kinetic coefficients. The analysis was performed by fitting the temporal evolution of the recrystallized fraction to the Avrami equation and extracting the half recrystallization fraction time for the different cases, as shown in Fig. 9. From this, several notes can be discerned. The first is in regard of the influence of the distribution sought to sample the boundary spacing. Unlike the Rayleigh distribution case, the equispaced dislocation wall simulation exhibits an initial decrease in the recrystallized fraction, followed by an increase to the asymptotic value of 1 because 5 out of the 10 seeded recrystallization nuclei embryos shrunk and disappeared, before a single recrystallized grain grows to occupy the entire deformed matrix. The latter can be interpreted considering the remarkable difference in the local stored energy in the vicinity of a single dislocation boundary with values higher by an order of magnitude than the homogenous case allowing the growth of recrystallized nuclei embryos with radius lower than the critical radius estimated for the case of a homogenous field. The increase in the magnitude of the deformation-energy across the dislocation boundary is more pronounced in the case of the Rayleigh distribution due to the statistical variation in the boundary spacing resulting in higher stored energy across the GNBs or increasing the number of GNBs intersecting the boundary of a single recrystallization nuclei. The second note to be made concerns the fast kinetics obtained by using the heterogeneous deformation-energy field as compared to the homogenous field. In this regard, the use of equispaced dislocation walls shows

559 behaviors closer to the homogenous deformation field. For example, the half recrystallization
560 fraction time in this case is larger than the Rayleigh distribution sampled spacing by a factor of
561 three. In addition, the recrystallization front seems smoother, and the growth seems more
562 symmetric, i.e., the preferential recrystallization front growth along the GNBs is less obvious. The
563 third note is about the kinetic parameters being sensitive to the smearing method of the
564 deformation-energy across the boundary, which evidences the importance of characterizing the
565 dislocation structure inside the boundaries to substantiate the energy representation across the
566 boundary based on real microstructure data. The last note concerns the one order of magnitude
567 decrease in the half recrystallization fraction time by assigning the cell a deformation-energy in
568 the high range. This suggests a crossover to a regime with the kinetics completely controlled by
569 the cell's interior energy instead of the dislocation boundary structure. This last note seems
570 consistent and in conformity with the asymptotic prediction based on the calculated values for the
571 domain-averaged deformation-energy density. In general, the half recrystallization fraction time is
572 found to increase exponentially with the deformation-energy density. On the same note, an
573 additional simulation was performed to investigate the impact of the IDB curvature on the
574 recrystallization kinetics at the lower strain, and no difference was observed. This suggests
575 recrystallization nuclei growth at low levels of strain is less sensitive to the morphology of the
576 IDBs and is mainly controlled by GNBs. It is worth mentioning that the simulated kinetics are
577 about one order of magnitude faster than some reported experimental values [31]. This could be
578 attributed to the use of a high initial nuclei density.
579

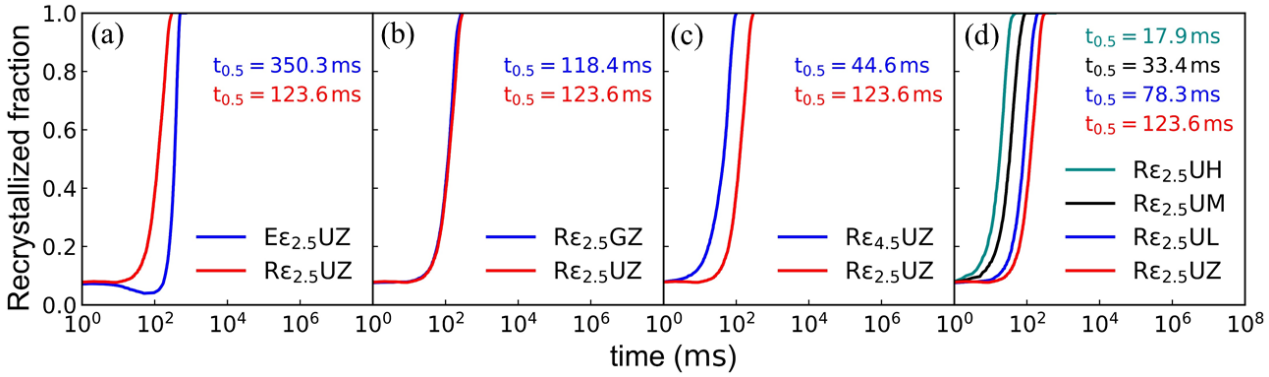

Fig. 9. Impact of various factors on the kinetics of recrystallization. (a) Boundary-spacing distribution for a given deformation energy density. (b) Energy smearing method across the boundaries. (c) Strain and (d) cell- energy density.

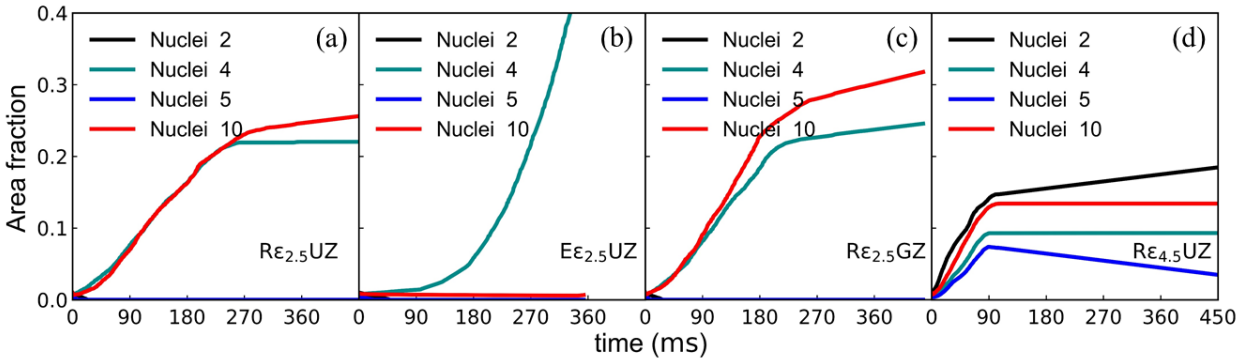

Fig. 10. Effect of the underlying deformed structure on the kinetics of the four nuclei shown in Fig. 2(b) for the initial arrangement of dislocation boundaries shown in Fig. 3.

The temporal evolution of the recrystallized fraction elucidates how in an overall sense recrystallization kinetics is dependent on microstructure heterogeneity, but to thoroughly understand the effects on individual nuclei we should track the temporal growth of the area fraction of individual nuclei, which are plotted in Fig. 10 and Fig. 11. The study of the kinetics of each nucleus helps in visualizing the impact of the recrystallization stage on the coarsening stage. Fig. 10(a,c) show the impact of energy smearing method across the boundaries on the individual nuclei and it is clear that the nuclei 4 and nuclei 2 are the active nuclei, among the reported, with the growth rate being higher in gaussian smearing method. The latter could be due to the larger spread of the elastic strain energy into the interiors of the cells leading to greater driving force for the

motion of the recrystallization front of the nuclei. Fig. 10(a,b) show the impact of spacing distribution on the kinetics of individual nuclei at the lower strain. As reported earlier, the dislocation boundary energies from Rayleigh spacing distributions provides greater driving force for the nuclei in comparison to the equispaced distribution, explaining the observed kinetics of individual nuclei. In Fig. 10(a,d) it is clear that increase in overall strain lead to growth of some nuclei, which shrunk to zero size in lower strain, due to reduced spacing between the boundaries and an increased boundary energy providing greater driving force for growth. As is clear from Fig. 11, assigning a non-zero energy density to the interiors of the cells can result in a completely different microstructure development in comparison to the case of zero deformation-energy density. For example, nuclei 2 only grows significantly in area when the values of the energy density assigned to the cell crosses some threshold value, which is evident from Fig. 11(c,d).

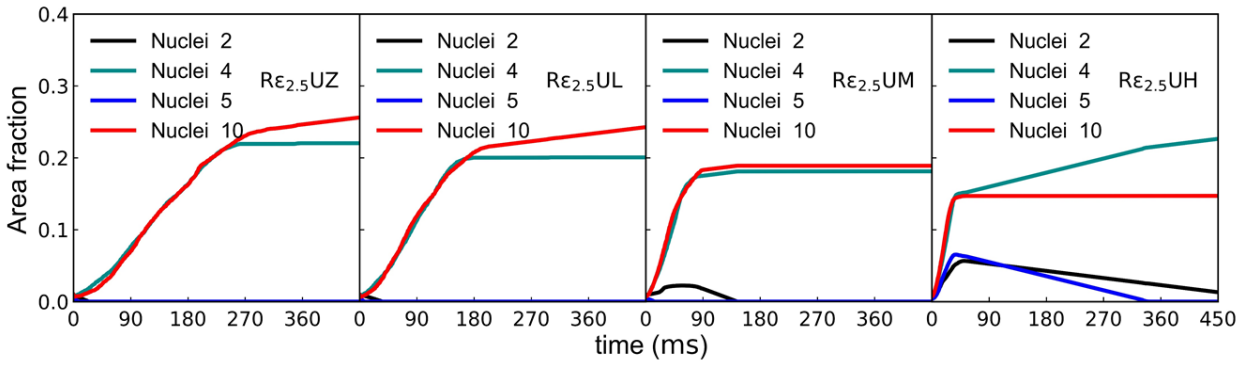

Fig. 11. Impact of non-zero deformation energy density in the interiors on the kinetics of individual nuclei for a Rayleigh distributed dislocation spacing and misorientation angles shown in Fig. 3b and Fig. 4(a-c).

From the presented results, it is comprehensible how the recrystallization kinetics and the recrystallization front are very sensitive to the local variation of the deformation-energy field. In addition, the heterogeneity in deformation-energy field plays a crucial role in determining the potential of recrystallization nuclei embryos to grow, and hence determines the final texture. All

these observations assert the extreme importance of the accurate description of the initial configuration of the heterogeneous deformation-energy field for reliable prediction of the microstructural evolution. The presented model for the deformation energy field successfully captures the observations made in experiments and sheds light on the influence that different variables have on the grain coarsening stage long after the end of the primary recrystallization stage. The findings from our work also captured the dependence of kinetics and final texture evolution on various parameters characterizing the heterogeneous deformation field. Thus, emphasizing the urgent need to incorporate a realistic representation for the initial configuration of the recrystallized nuclei instead of the wide-spread approach of choosing simple structures. This of course suggests adopting experimental data characterizing the size and orientation distribution of the initial nuclei as well as their preferred sites. Moreover, as was demonstrated by the simulation results, the lack of accountability to the misorientation dependence of the grain boundary mobility can lead to the prediction of drastically different microstructures.

5. Summary and Outlook

To summarize, the dislocation patterns observed experimentally after the recovery stage of plastically deformed metals (deformation structures) can be described quantitatively in terms of microstructural parameters associated with the deformed state. These patterns determine the local variation of the deformation-energy field, which is proven to play a vital rule controlling the recrystallization kinetics, any emerging texture, and the final grain structure. Deformation induces a dislocation cell structure in metals with medium to high SFE. The scaling behavior of the spatial distributions of dislocation wall spacing (IDBs and GNBs, delineating the equiaxed cells and the cell blocks, respectively) and their misorientation angles makes it possible to capture the heterogeneity in real deformation microstructures by merely determining the average

misorientation angles and wall spacings, which are functions of the strain. By applying these scaling laws, an initial configuration for recrystallization simulation can be derived on a physical basis. Consequently, the sensitivity of recrystallization kinetics to the local spatial variation of deformation-energy can be accurately modelled at the length scale of the dislocation cell size for the plastic strain range studied. This, in turn, paves the way for reliable prediction of the microstructural evolution during recrystallization through developing more realistic models that can accommodate the heterogenous nature of recrystallization nucleation.

The model developed here is unique in its way to make a direct connection with the universal scaling laws and the sampling of the deformation-energy from the experimentally observed statistical distributions, instead of grain-averaged parameters, thus resolving sub-grain structure. Thus, the model makes a better use of the available experimental data by resolving more details and provides flexibility in the assignment of the deformation-energy field allowing a realistic representation of the underlying structure. The model is parameterized using typical experimental values for FCC metals.

The present study demonstrates the direct connection between the heterogeneity of the deformation-energy field and several characteristic aspects of recrystallization phenomena observed experimentally, which are captured successfully in the simulation results. For example, the non-smooth morphology of recrystallization front exhibiting protrusions and retrusions was an obvious feature in all simulations. In addition, the results show the existence of preferential orientations for the growth of recrystallization nuclei along the GNBs, particularly at the lower strain where the energy across the GNBs is comparably higher with respect to IDBs. Moreover, the heterogenous representation of the deformation-energy-field reveals the sensitivity of the preexisting recrystallization nuclei to the local environment, which controls their growth rate and

survival odds. This, in turn, determines the final texture and grain structure, which is demonstrated to be a function of the deformed state.

The current investigation made it evident that accounting for deformation state is crucial in modelling recrystallization phenomena. However, several improvements are still needed to render any model predictions quantitatively reliable. For example, the contribution of long-range dislocation interaction to the deformation-energy field should be considered. For this purpose, an approach coupling phase-field and elasticity theory can be sought. In addition, a statistical model to describe the initial recrystallization nuclei configuration based on experimental findings needs to be developed. Future directions can also include the consideration of the anisotropy of the grain boundary mobility and its dependence on the misorientation angle. It is worth noting the anisotropy of grain boundary mobility could be important in the case of a highly anisotropic system and special grain boundaries. The relation between the orientations of the deformation-induced dislocation microstructure/boundaries and the sample crystallographic orientations, the dislocation contents of these boundaries, and the extent of the deformation-energy field across the boundaries, and last but not least, cell-energy, are all among the crucial parameters that need reliable determination. Furthermore, from a numerical perspective, assessing the sensitivity of the simulated kinetics to the choice of the interpolation function employed in the definition of the stored energy in the phase-field model and uncertainty quantification of the computed results should be eventually conducted.

Declaration of Competing Interest

The authors declare that they have no known competing financial interests or personal relationships that could have appeared to influence the work reported in this paper.

Acknowledgements

This work was supported by DOE-NE-In-pile instrumentation program at Idaho National Laboratory through a subcontract at Purdue University. A.E. acknowledges the support from the US Department of Energy, Office of Science, Division of Materials Sciences and Engineering, through award number DE-SC0017718, and from the National Science Foundation, Division of Civil, Mechanical, and Manufacturing Innovation (CMMI), through award number 1663311 at Purdue University.

References

[1] R.D. Doherty, D.A. Hughes, F.J. Humphreys, J.J. Jonas, D.J. Jensen, M.E. Kassner, W.E. King, T.R. McNelley, H.J. McQueen, A.D. Rollett, Current issues in recrystallization: a review, Materials Science and Engineering: A. 238 (1997) 219–274. https://doi.org/10.1016/S0921-5093(97)00424-3.

[2] P.R. Rios, F. Siciliano Jr, H.R.Z. Sandim, R.L. Plaut, A.F. Padilha, Nucleation and growth during recrystallization, Materials Research. 8 (2005) 225–238. https://doi.org/10.1590/S1516-14392005000300002.

[3] K. Huang, R.E. Logé, A review of dynamic recrystallization phenomena in metallic materials, Mater Des. 111 (2016) 548–574. https://doi.org/10.1016/j.matdes.2016.09.012.

[4] M. Azarbarmas, M. Aghaie-Khafri, J.M. Cabrera, J. Calvo, Dynamic recrystallization mechanisms and twining evolution during hot deformation of Inconel 718, Materials Science and Engineering A. 678 (2016) 137–152. https://doi.org/10.1016/j.msea.2016.09.100.

[5] A.D. (Anthony D.) Rollett, G.S. Rohrer, F.J. Humphreys, Recrystallization and related annealing phenomena., 2017. https://www.sciencedirect.com/book/9780080982359/recrystallization-and-related-annealing-phenomena#book-description (accessed April 3, 2018).

[6] N. Hansen, D. Juul Jensen, Deformed metals - Structure, recrystallisation and strength, Materials Science and Technology. 27 (2011) 1229–1240. https://doi.org/10.1179/1743284711Y.0000000046.

[7] D.A. Hughes, N. Hansen, Plastic deformation structures, Metallography and Microstructures. 9 (2004) 192–206. https://doi.org/10.1361/asmhba0003742.

[8] D.A. Hughes, N. Hansen, D.J. Bammann, Geometrically necessary boundaries, incidental dislocation boundaries and geometrically necessary dislocations, Scr Mater. 48 (2003) 147–153. https://doi.org/10.1016/S1359-6462(02)00358-5.

[9] R.D. Doherty, The Deformed State and Nucleation of Recrystallization, Metal Science. 8 (1974) 132–142. https://doi.org/10.1179/msc.1974.8.1.132.

[10] C. Xu, Y. Zhang, A. Godfrey, G. Wu, W. Liu, J.Z. Tischler, Q. Liu, D.J. Jensen, Direct observation of nucleation in the bulk of an opaque sample, Sci Rep. 7 (2017) 1–7. https://doi.org/10.1038/srep42508.

[11] Y. Shibuta, S. Sakane, E. Miyoshi, S. Okita, T. Takaki, M. Ohno, Heterogeneity in homogeneous nucleation from billion-atom molecular dynamics simulation of solidification of pure metal, Nat Commun. 8 (2017) 1–8. https://doi.org/10.1038/s41467-017-00017-5.

[12] A. Godfrey, O. v Mishin, T. Yu, Characterization and influence of deformation microstructure heterogeneity on recrystallization, IOP Conf Ser Mater Sci Eng. 89 (2015) 012003. https://doi.org/10.1088/1757-899X/89/1/012003.

[13] A. Oudriss, X. Feaugas, Length scales and scaling laws for dislocation cells developed during monotonic deformation of (001) nickel single crystal, Int J Plast. 78 (2016) 187–202. https://doi.org/10.1016/j.ijplas.2015.11.003.

[14] A. Godfrey, D.A. Hughes, Scaling of the spacing of deformation induced dislocation boundaries, Acta Mater. 48 (2000) 1897–1905. https://doi.org/10.1016/S1359-6454(99)00474-7.

[15] W.T. Read, W. Shockley, Dislocation Models of Crystal Grain Boundaries, Phys. Rev. 78 (1950) 275–289. https://doi.org/10.1103/PhysRev.78.275.

[16] A. Godfrey, W.Q. Cao, Q. Liu, N. Hansen, Stored energy, microstructure, and flow stress of deformed metals, Metallurgical and Materials Transactions A. 36 (2005) 2371–2378. https://doi.org/10.1007/s11661-005-0109-0.

[17] P. Zhitelev, A. Vasilyev, S. Sokolov, D. Sokolov, R. Paligin, Investigation and modeling of recrystallization of cold rolled automotive steels, IOP Conf Ser Mater Sci Eng. 124 (2016). https://doi.org/10.1088/1757-899X/124/1/012112.

[18] H. Hallberg, Approaches to modeling of recrystallization, Metals (Basel). 1 (2011) 16–48. https://doi.org/10.3390/met1010016.

[19] A.D. Rollett, D. Raabe, A hybrid model for mesoscopic simulation of recrystallization, n.d. www.elsevier.com/locate/commatsci.

[20] D.Q. Duan, W.P. Yang, X. Liu, D.M. Liu, Three-dimensional Monte Carlo simulation of recrystallization in silver, in: Proceedings of the 2011 International Conference on Business Computing and Global Informatization, BCGIn 2011, 2011: pp. 416–419. https://doi.org/10.1109/BCGIn.2011.110.

[21] S.M.A. Khan, H.M. Zbib, D.A. Hughes, Modeling planar dislocation boundaries using multi-scale dislocation dynamics plasticity, Int J Plast. 20 (2004) 1059–1092. https://doi.org/10.1016/j.ijplas.2003.10.004.

[22] S.M.A. Khan, Multi-scale modeling of dislocation boundaries: Understanding interaction and effect of rotation angle, Comput Mater Sci. 95 (2014) 435–439. https://doi.org/10.1016/j.commatsci.2014.08.006.

[23] M.A. Miodownik, E.A. Holm, A.W. Godfrey, D.A. Hughes, R. Lesar, Multiscale Modeling of Recrystallization, in: Mat. Res. Soc. Symp., 1999: pp. 157–162.

[24] J. de Jaeger, D. Solas, O. Fandeur, J.H. Schmitt, C. Rey, 3D numerical modeling of dynamic recrystallization under hot working: Application to Inconel 718, Materials Science and Engineering A. 646 (2015) 33–44. https://doi.org/10.1016/j.msea.2015.08.038.

[25] I. Steinbach, Phase-field models in materials science, Model Simul Mat Sci Eng. 17 (2009). https://doi.org/10.1088/0965-0393/17/7/073001.

[26] L.-Q. Chen, Phase-Field Models for Microstructure Evolution, Annu Rev Mater Res. 32 (2002) 113–140. https://doi.org/10.1146/annurev.matsci.32.112001.132041.

[27] N. Moelans, B. Blanpain, P. Wollants, An introduction to phase-field modeling of microstructure evolution, CALPHAD. 32 (2008) 268–294. https://doi.org/10.1016/j.calphad.2007.11.003.

[28] N. Moelans, B. Blanpain, P. Wollants, Quantitative analysis of grain boundary properties in a generalized phase field model for grain growth in anisotropic systems, Phys Rev B Condens Matter Mater Phys. 78 (2008). https://doi.org/10.1103/PhysRevB.78.024113.

[29] N. Moelans, A. Godfrey, Y. Zhang, D. Juul Jensen, Phase-field simulation study of the migration of recrystallization boundaries, Phys Rev B Condens Matter Mater Phys. 88 (2013) 1–10. https://doi.org/10.1103/PhysRevB.88.054103.

[30] N. Moelans, Y.B. Zhang, A. Godfrey, D.J. Jensen, A phase-field simulation study of irregular grain boundary migration during recrystallization, IOP Conf Ser Mater Sci Eng. 89 (2015). https://doi.org/10.1088/1757-899X/89/1/012037.

[31] S.P. Gentry, K. Thornton, Simulating recrystallization in titanium using the phase field method, IOP Conf Ser Mater Sci Eng. 89 (2015). https://doi.org/10.1088/1757-899X/89/1/012024.

[32] C.N. Athreya, A. Mukilventhan, S. Suwas, S. Vedantam, V. Subramanya Sarma, Influence of the mode of deformation on recrystallisation kinetics in Nickel through experiments, theory and phase field model, Philosophical Magazine. 97 (2017) 3211–3228. https://doi.org/10.1080/14786435.2017.1370146.

[33] S. Sreekala, M. Haataja, Recrystallization kinetics: A coupled coarse-grained dislocation density and phase-field approach, Phys Rev B Condens Matter Mater Phys. 76 (2007) 1–13. https://doi.org/10.1103/PhysRevB.76.094109.

[34] C. Yoshimoto, T. Takaki, Multiscale Hot-working Simulations Using Multi-phase-field and Finite Element Dynamic Recrystallization Model, ISIJ International. 54 (2014) 452–459. https://doi.org/10.2355/isijinternational.54.452.

[35] E. Miyoshi, T. Takaki, Extended higher-order multi-phase-field model for three-dimensional anisotropic-grain-growth simulations, Comput Mater Sci. 120 (2016) 77–83. https://doi.org/10.1016/j.commatsci.2016.04.014.

[36] E. Miyoshi, T. Takaki, Validation of a novel higher-order multi-phase-field model for grain-growth simulations using anisotropic grain-boundary properties, Comput Mater Sci. 112 (2016) 44–51. https://doi.org/10.1016/j.commatsci.2015.10.010.

[37] J.-S. Zhang, Evolution of Dislocation Substructures During Creep, in: High Temperature Deformation and Fracture of Materials, Elsevier, 2010: pp. 14–27. https://doi.org/10.1533/9780857090805.1.14.

[38] D.A. Hughes, N. Hansen, The microstructural origin of work hardening stages, Acta Mater. 148 (2018) 374–383. https://doi.org/10.1016/j.actamat.2018.02.002.

[39] Y. Zhang, A. Godfrey, D. Juul Jensen, In-situ investigation of local boundary migration during recrystallization, Metall Mater Trans A Phys Metall Mater Sci. 45 (2014) 2899–2905. https://doi.org/10.1007/s11661-014-2222-4.

[40] Y. Zhang, A. Godfrey, N. MacDonald, D.J. Jensen, 3D Characterization of Recrystallization Boundaries, in: Proceedings of the 1st International Conference on 3D Materials Science, Springer International Publishing, Cham, 2012: pp. 31–36. https://doi.org/10.1007/978-3-319-48762-5_5.

[41] D.A. Hughes, N. Hansen, Plastic Deformation Structures, in: Metallography and Microstructures, ASM International, 2018: pp. 192–206. https://doi.org/10.31399/asm.hb.v09.a0003742.

[42] Y. Zhang, A. Godfrey, D.J. Jensen, Local boundary migration during recrystallization in pure aluminium, Scr Mater. 64 (2011) 331–334. https://doi.org/10.1016/j.scriptamat.2010.10.028.

[43] M.A. Martorano, H.R.Z. Sandim, M.A. Fortes, A.F. Padilha, Observations of grain boundary protrusions in static recrystallization of high-purity bcc metals, Scr Mater. 56 (2007) 903–906. https://doi.org/10.1016/j.scriptamat.2007.01.032.

[44] D.A. Hughes, N. Hansen, The microstructural origin of work hardening stages, Acta Mater. 148 (2018) 374–383. https://doi.org/10.1016/j.actamat.2018.02.002.

[45] V. Vivekanandan, P. Lin, G. Winther, A. El-Azab, On the implementation of dislocation reactions in continuum dislocation dynamics modeling of mesoscale plasticity, J Mech Phys Solids. 149 (2021). https://doi.org/10.1016/j.jmps.2021.104327.

[46] V. Yadav, N. Moelans, Y. Zhang, D. Juul Jensen, Influence of geometrical alignment of the deformation microstructure on local migration of grain boundaries during recrystallization: A phase-field study, Scr Mater. 191 (2021) 116–119. https://doi.org/10.1016/j.scriptamat.2020.09.028.

[47] V. Yadav, N. Moelans, Y. Zhang, D. Juul Jensen, Effects of dislocation boundary spacings and stored energy on boundary migration during recrystallization: A phase-field analysis, Acta Mater. 221 (2021). https://doi.org/10.1016/j.actamat.2021.117377.

[48] D.A. Hughes, N. Hansen, Microstructure and strength of nickel at large strains, Acta Mater. 48 (2000) 2985–3004. https://doi.org/10.1016/S1359-6454(00)00082-3.

[49] D.A. Hughes, S.M.A. Khan, A. Godfrey, H.M. Zbib, Internal structures of deformation induced planar dislocation boundaries, Materials Science and Engineering A. 309–310 (2001) 220–226. https://doi.org/10.1016/S0921-5093(00)01691-9.

[50] P.J. Hurley, F.J. Humphreys, The application of EBSD to the study of substructural development in a cold rolled single-phase aluminium alloy, Acta Mater. 51 (2003) 1087–1102. https://doi.org/10.1016/S1359-6454(02)00513-X.

[51] B.P. Kashyap, Deformation microstructures and selected examples of their recrystallization, Surface and Interface Analysis. 31 (2001) 560–570. https://doi.org/10.1002/sia.1083.

[52] O. v. Mishin, Y.B. Zhang, A. Godfrey, The influence of multiscale heterogeneity on recrystallization in nickel processed by accumulative roll bonding, J Mater Sci. 52 (2017) 2730–2745. https://doi.org/10.1007/s10853-016-0566-4.

[53] X. Huang, A. Borrego, W. Pantleon, Polycrystal deformation and single crystal deformation: Dislocation structure and flow stress in copper, Materials Science and Engineering A. 319–321 (2001) 237–241. https://doi.org/10.1016/S0921-5093(01)01019-X.

[54] E.C. Aifantis, The physics of plastic deformation, Int J Plast. 3 (1987) 211–247. https://doi.org/10.1016/0749-6419(87)90021-0.

[55] B. Bay, N. Hansen, D.A. Hughes, D. Kuhlmann-Wilsdorf, Overview no. 96 evolution of f.c.c. deformation structures in polyslip, Acta Metallurgica Et Materialia. 40 (1992) 205–219. https://doi.org/10.1016/0956-7151(92)90296-Q.

[56] G. Abrivard, E.P. Busso, S. Forest, B. Appolaire, Phase field modelling of grain boundary motion driven by curvature and stored energy gradients. Part II: Application to recrystallisation, in: Philosophical Magazine, 2012: pp. 3643–3664. https://doi.org/10.1080/14786435.2012.717726.

[57] G. Abrivard, E.P. Busso, S. Forest, B. Appolaire, Phase field modelling of grain boundary motion driven by curvature and stored energy gradients. Part I: Theory and numerical implementation, in: Philosophical Magazine, 2012: pp. 3618–3642. https://doi.org/10.1080/14786435.2012.713135.

[58] C.J. Permann, D.R. Gaston, D. Andrš, R.W. Carlsen, F. Kong, A.D. Lindsay, J.M. Miller, J.W. Peterson, A.E. Slaughter, R.H. Stogner, R.C. Martineau, MOOSE: Enabling massively parallel multiphysics simulation, SoftwareX. 11 (2020) 100430. https://doi.org/10.1016/j.softx.2020.100430.

[59] C.A. Schneider, W.S. Rasband, K.W. Eliceiri, NIH Image to ImageJ: 25 years of image analysis, Nat Methods. 9 (2012) 671–675. https://doi.org/10.1038/nmeth.2089.